Supplementary material

Multifunctional flexible ferroelectric thick-film structures with energy storage, piezoelectric and electrocaloric performance

Matej Sadl[1,2], Uros Prah[3], Veronika Kovacova[3], Emmanuel Defay[3], Tadej Rojac[1,2], Andrej Lebar[4,5], Josko Valentincic[4], and Hana Ursic[1,2,*]

[1]Electronic Ceramics Department, Jožef Stefan Institute, Jamova cesta 39, 1000 Ljubljana, Slovenia;

[2]Jožef Stefan International Postgraduate School, Jamova cesta 39, 1000 Ljubljana, Slovenia;

[3]Materials Research and Technology Department, Luxembourg Institute of Science and Technology, Belvaux, Luxembourg;

[4]Faculty of Mechanical Engineering, University of Ljubljana, Aškerčeva cesta 6, 1000 Ljubljana, Slovenia;

[5]Faculty of Health Sciences, University of Ljubljana, Zdravstvena pot 5, 1000 Ljubljana, Slovenia.

*Correspondence: hana.ursic@ijs.si

Table of Content

S1: Aerosol deposition process parameters

Table S1: Process parameters used during the AD.

Process Parameters	
Carrier gas species	N_2
Nozzle geometry (slit size)	(0.5 × 10) mm^2
Distance between nozzle and substrate	5 mm
Sweep speed	5 $mm \cdot s^{-1}$
Gas flow rate	4 $L \cdot min^{-1}$
Pressure in aerosol chamber	180 mbar
Pressure in deposition chamber	2 mbar

S2: Rietveld refinement analysis

A quantitative analysis of the XRD data was performed using the Rietveld refinement method. The measured XRD patterns and the corresponding calculated profiles after Rietveld refinement of the PMN–35PT powder, as-deposited thick film and thermally annealed thick film are shown in Figure S2. The agreement factors and unit cell parameters of the Rietveld refinement are listed in Table S2.

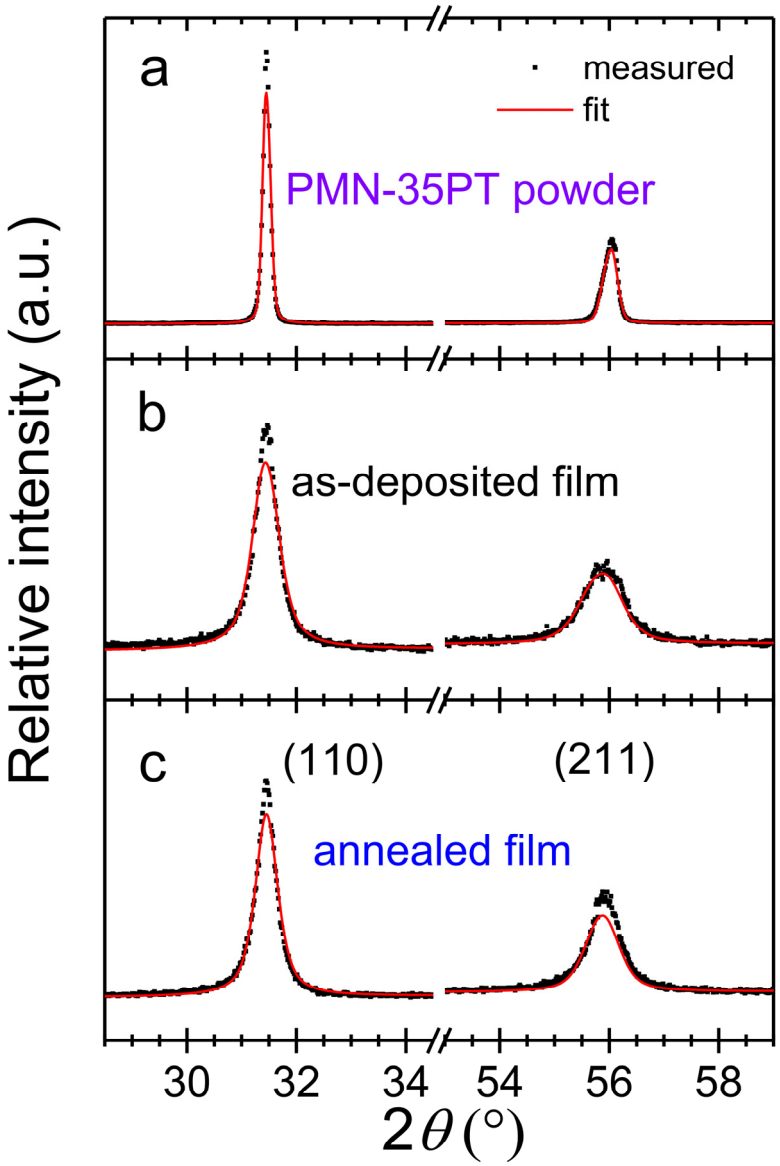

Figure S2: The measured XRD patterns (black) and the corresponding calculated profiles (red) of (110) and (211) PMN–35PT reflections for (a) PMN–35PT powder, (b) as-deposited thick film and (c) annealed thick film.

Table S2: Agreement factors of the Rietveld refinement analysis.

Sample	PMN–35PT powder	As-deposited film	Annealed film
Crystal system	Tetragonal	Tetragonal	Tetragonal
Space group	*P*4*mm*	*P*4*mm*	*P*4*mm*
a (Å)	4.010987(75)	4.02379(35)	4.02885(46)
c (Å)	4.03041(11)	4.06755(73)	4.05415(96)
R_{wp} (%)	14.49	13.41	14.93
R_{exp} (%)	10.28	10.75	10.91
R_p (%)	11.47	10.03	10.97
G. O. F.	1.41	1.25	1.37

S3: Bending strain

The bending strain of the thick film surface dependents on the bend curvature and was calculated by using the multilayer model [1], [2]. In the thick film multilayer structure there is a neutral mechanical plane, where the bending strain is zero (Figure S3). The distance between the neutral mechanical plane and the film surface is given by equation (S3.1):

$$b = \frac{\sum_{i=1}^{N} \bar{E}_i \, h_i \left[\left(\sum_{j=1}^{i} h_j \right) - \frac{h_i}{2} \right]}{\sum_{i=1}^{N} \bar{E}_i \, h_i} \qquad \text{(S3.1)}$$

where N is the total number of layers and h_i is the thickness of the i^{th} layer (from the top). $\bar{E}_i$ is equal to $E_i/(1-\nu_i^2)$, where E_i and ν_i are Young's modulus and Poisson's ratio of the i^{th} layer, respectively.

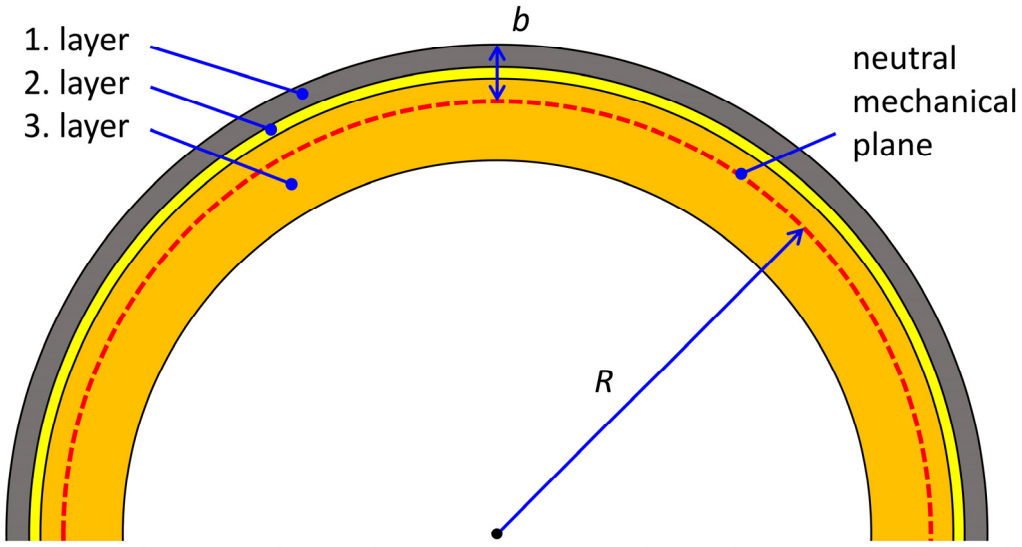

Figure S3: A scheme of a multilayer structure under bending. The 1. layer experiences a tensile bending strain, while the neutral mechanical plane (red dashed line) has zero bending strain. The scheme is not to scale.

The bending strain in the multilayer structure can be calculated by equation (S3.2):

$$\varepsilon = \frac{y}{R} \qquad \text{(S3.2)}$$

where R is the bend radius and y the distance from the neutral mechanical plane. Thus, the highest bending strains are on the film's surface, where y equals b. All parameters needed for the calculation of the bending strain are given in the Table S3.1. E_i and ν_i values were taken from the references given in the same Table S3.1. Note, that the Young's modulus of AD thick films depends on the thermal treatment, which was confirmed for aerosol-deposited $BaTiO_3$ thick films annealed at 500 °C [3]. After annealing of $BaTiO_3$ thick films at 500 °C, the Young's modulus increased by about 15%. However, since there are no similar studies on aerosol-deposited PMN–35PT thick films, we did not consider the changes in Young's modulus after annealing. The calculated bending strain for different bending radii used in the evaluation of flexibility can be found in Table S3.2.

Table S3.1: Elastic properties and layer thicknesses.

i	1	2	3
layer	PMN–35PT thick film	Au bottom electrode	polyimide substrate (Kapton® HN)
h_i (µm)	2.5	1.2	125
E_i (GPa)	90	78	2.76
ν_i	0.30	0.43	0.34
reference	[4]	[5]	[6]

Table S3.2: The calculated bending strain for different bending radii.

Bending radius (mm)	Bending strain (%)
12	0.29
10	0.35
7.5	0.47
5.0	0.71
4.0	0.88
3.0	1.18
1.5	2.35

S4: EC measurements

EC measurements of as-deposited PMN–35PT thick films

The EC measurement with a calorimeter method performed on the as-deposited PMN–35PT thick films show a strong Joule heating. The thermistor temperature vs. time is plotted in Figure S4.1. The electric field amplitude of the square-like waveform was progressively increased from 50 to 250 kV·cm^{-1}. From 100 kV·cm^{-1} onwards the temperature of the thick film samples (during the 100 s on-field) increases due to the Joule heating effect, indicating a sudden increase in electrical conductivity. For this reason, the EC effect could not be reliably measured for the as-deposited PMN–35PT thick films.

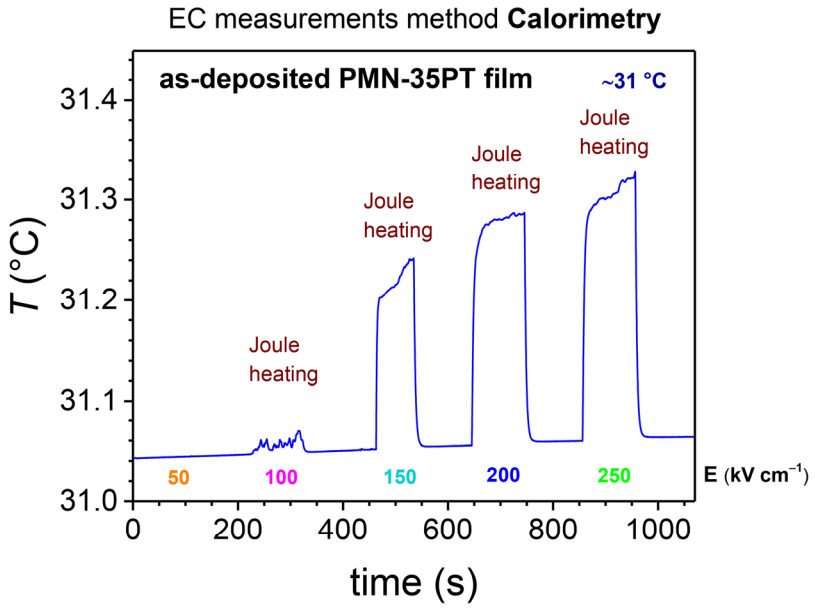

Figure S4.1: Time dependent temperature measurement of as-deposited PMN–35PT thick films using calorimetry. Joule heating was observed during 100 s on-field periods.

EC measurements of thermally annealed PMN–35PT thick films

The evaluated temperature changes (ΔT) of the thermally annealed PMN–35PT thick film measured by the calorimetry and the IR camera method are shown in Figure S4.2(a) and (b), respectively.

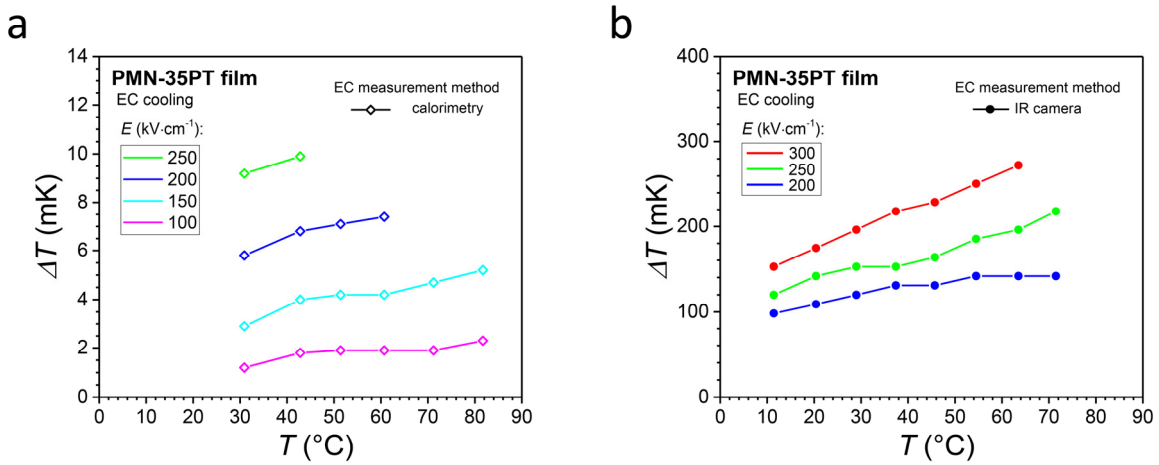

Figure S4.2: Temperature- and electric field-dependent ΔT measured on the annealed PMN–35PT thick film using (a) calorimetry and (b) IR camera method. Note the difference in the scales of ΔT.

To evaluate the intrinsic EC temperature change (ΔT_{EC}) of the PMN–35PT film, the measured ΔT was multiplied by a correction factor (k) specific to each method. For the IR camera method, a k was determined by numerical modelling of heat dissipation during the EC cycle (see ref. [7] for details), and for the calorimetry, a k was determined by the heat capacity analysis described below.

Evaluation of the correction factor for the EC measurements with a calorimeter method

For the EC measurement using calorimetry, the ΔT_{EC} of the PMN–35PT film alone cannot be detected by the thermistor because the thermalization time is too long. Nevertheless, the thermistor detects the temperature change ΔT of the entire sample structure (i.e., active PMN–35PT film, non-active PMN–35PT film, substrate, bottom Au electrode, top Au electrode, Cu wires, thermistor, adhesive for the Cu wires and adhesive for the thermistor) assuming rapid internal thermal relaxation. Thus, the ΔT_{EC} can be calculated by knowing the ratio between the heat capacity of all components in the sample structure $\sum_i C_p^i$ and the heat capacity of the active film (under the top electrode) C_p^{EC} (equation S4.1) [8]. This ratio is often referred to as the correction factor (k). The heat capacity of all components in the sample structure at room temperature are shown in Table S4.1.

$$\Delta T_{EC} = \frac{\sum_i C_p^i}{C_p^{EC}} \cdot \Delta T = k \cdot \Delta T \qquad \text{(S4.1)}$$

Table S4.1: The components of the whole sample structure, their heat capacity and the calculated *k* at room temperature.

Component	Heat capacity (mJ·K^{-1})
Adhesive for Cu wires	0.0238
Adhesive for thermistor	0.2841
Thermistor	0.0794
Cu wires	0.3542
Top Au electrode	0.0018
Bottom Au electrode	0.0649
Active PMN–35PT film - C_p^{EC}	0.0745
Non-active PMN-35PT film	0.1428
Substrate	3.7604
Total - $\sum_i C_p^i$	4.7860
k = 64	

Assessment of measurement uncertainty for the EC measurements with the IR camera method

For the IR camera method, the analysis of the measurement uncertainty of the obtained adiabatic ΔT_{EC} was performed considering two main contributions, i.e., the measured ΔT and the obtained k, according to equation S4.1. The evaluation was based on three different EC cycles measured at three different temperatures (namely ~20.4 °C, ~45.7 °C, and ~63.5 °C) and 300 kV·cm^{-1} (Figure S4.3a).

The first contribution to the measurement uncertainty of the ΔT determination is related to the variation of the temperature measurement by the IR camera, as can be seen from the base temperature (thermalized part of the EC cycle) in Figure S4.3a and S4.3b. A quite high measurement noise is related to the free air environment (hot plate structure) and the limited thermal sensitivity of the measurement setup. All contributions to the total measurement uncertainty along with the mean ($\bar{X}$), standard deviation (σ) and relative standard deviation (σ_R) values are summarized in Table S4.2. The σ of the measured temperature from a selected baseline (Figure S4.3b) reaches the values up to 30 mK, which can be considered as the resolution of the IR camera. Considering the σ of the measured temperature, σ increases to 40 mK for the determination of ΔT (marked as contribution 1 in Table S4.2). In addition, the variation of ΔT_{cycles} resulting from several measured EC cycles, which represents the repeatability of the obtained EC cooling peaks (Figure S4.3a), was included to estimate the overall uncertainty of the measured ΔT. σ of the ΔT_{cycles} obtained for three consecutive cooling peaks was 20 mK (contribution 2 in Table S4.2). The combination of both contributions (1+2 in Table S4.2) representing the measured ΔT gave σ of 40–50 mK.

Another source of measurement uncertainty is the determination of the correction factor. Compared to temperature measurements, it is somewhat more difficult to determine and quantify the degree of uncertainty for k. The main sources of error are probably related to the uncertainty in determining the thickness of the active ceramic film and the printed black ink, the determination of the thermal

parameters used in the numerical modelling, and the error in fitting the numerical model to the experimental data. In this case, the σ_R in the determination of k was estimated to be up to 10% (contribution 3 in Table S4.2).

The combination of all three contributions described above (1+2+3 in Table S4.2) resulted in an overall σ_R of the adiabatic ΔT_{EC} obtained by the IR camera method between 18% and 29%. Despite the assumption of a relatively large σ_R for k of 10%, the main contribution to the overall measurement uncertainty comes from the large temperature variations detected by the IR camera. However, the measurement uncertainty depends strongly on the amplitude of the measured EC effect, which can be significantly improved by larger EC temperature difference and thus a larger signal-to-noise ratio.

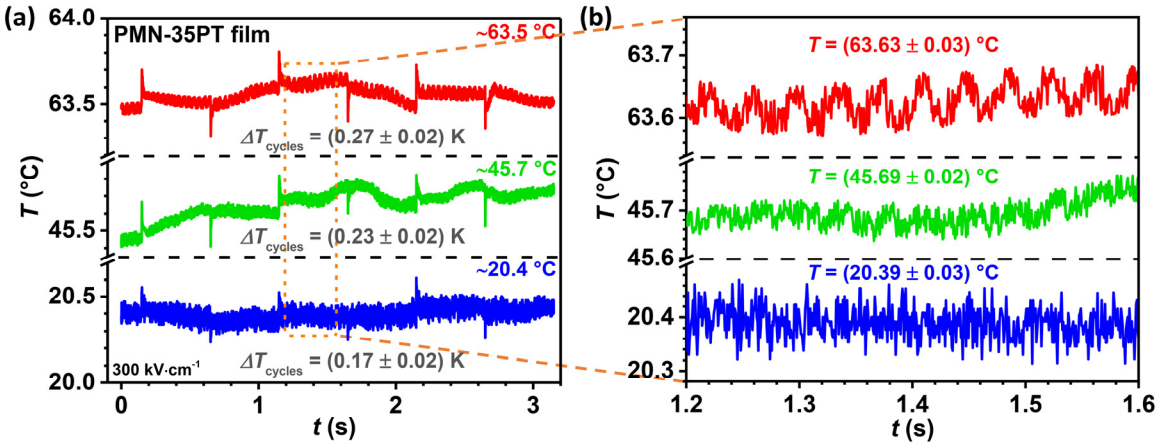

Figure S4.3: (a) Sequence of three EC cycles measured with the IR camera at different ambient temperatures and 300 kV·cm^{-1}, with (b) magnified view of a selected temperature range used to determine the σ of the temperature.

Table S4.2: Individual contributions and total measurement uncertainty of the ΔT_{EC} determined with the IR camera method.

Contribution to measurement uncertainty (IR camera method)		~20.4 °C (300 kV·cm^{-1})			~45.7 °C (300 kV·cm^{-1})			~63.5 °C (300 kV·cm^{-1})		
		$\bar{X}$	σ	σ_R	$\bar{X}$	σ	σ_R	$\bar{X}$	σ	σ_R
1	T	/	0.03 K	/	/	0.02 K	/	/	0.03 K	/
	ΔT	/	0.04 K	/	/	0.03 K	/	/	0.04 K	/
2	ΔT_{cycles}	0.17	0.02 K	12%	0.23	0.02 K	9%	0.27	0.02 K	7%
3	k	3.20	0.32	10%	3.20	0.32	10%	3.20	0.32	10%
1+2		0.17	0.05 K	28%	0.23	0.04 K	16%	0.27	0.04 K	16%
1+2+3	ΔT_{EC}	0.54	0.16 K	**29%**	0.74	0.14 K	**19%**	0.86	0.16 K	**18%**

Assessment of measurement uncertainty for the EC measurements with the calorimeter method

For the calorimeter method, the analysis of the measurement uncertainty of the obtained adiabatic ΔT_{EC} was performed considering two contributions, i.e., the measured ΔT and the obtained correction factor (k), according to equation S4.1. The evaluation was based on an EC cycle measured at three different temperatures (namely ~30.9 °C, ~42.8 °C, and ~60.7 °C) and 200 kV·cm^{-1} (Figure S4.4). All contributions to the total measurement uncertainty along with the mean ($\bar{X}$), standard deviation (σ) and relative standard deviation (σ_R) values are summarized in Table S4.3.

The first contribution considered in the measurement uncertainty is related to the measured T of thermistor. From the variation of base temperature (the noise of the thermalized part of the EC cycle), a σ was evaluated, which reaches 0.15 mK (Figure S4.4). The variation of the base temperature contributes to the uncertainty in the determination of the temperature difference, so that the σ for the determination of ΔT reaches 0.21 mK, which corresponds to 2.8–3.6% of the σ_R (contribution 1, Table S4.3).

The second contribution that must be taken into account in the measurement uncertainty results from the determination of the correction factor. The correction factor is calculated from the heat capacity of the individual sample components (Table S4.1), which is determined by measuring various quantities such as mass, volume, density and specific heat capacity. To evaluate the σ of the correction factor, we tracked the σ for the heat capacity of each individual sample component. The RSD in the determination of k reaches 21% (contribution 2, Table S4.3), regardless of temperature.

For the calorimeter method, a combination of the two contributions described above (1+2 in Table S4.3) resulted in an overall measurement uncertainty of the adiabatic ΔT_{EC}, i.e., the σ_R of 21%. Note that the uncertainty of the ΔT makes a negligible contribution and the uncertainty of k dominates the total measurement uncertainty of ΔT_{EC}. Other factors that may also affect the uncertainty of the calorimeter method are: a) the heat transfer between the thermistor and the sample surface, which is affected by the amount of adhesive between the thermistor and the sample surface, b) the temperature gradient in the sample due to an inhomogeneous heat distribution.

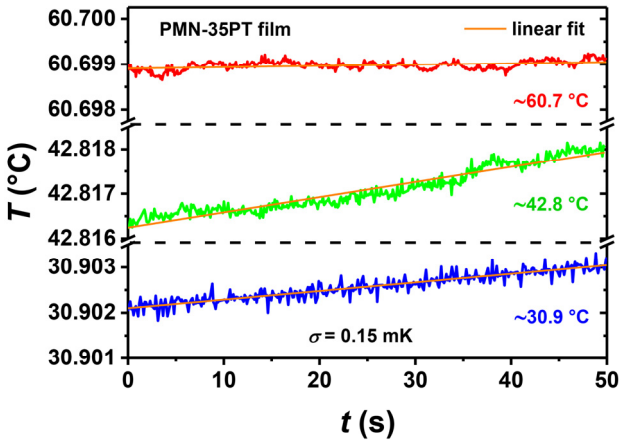

Figure S4.4: Thermalization temperature of the EC cycle in the calorimeter method at three different temperatures (~30.9 °C, ~42.8 °C, and ~60.7 °C) and 200 kV·cm^{-1}. The standard deviation (σ) of the signal was evaluated by consider a linear fit.

Table S4.3: Individual contributions and total measurement uncertainty of the ΔT_{EC} determined with the calorimeter method.

Contribution to measurement uncertainty (calorimeter method)		~30.9 °C (200 kV·cm^{-1})			~42.8 °C (200 kV·cm^{-1})			~60.7 °C (200 kV·cm^{-1})		
		$\bar{X}$	σ	σ_R	$\bar{X}$	σ	σ_R	$\bar{X}$	σ	σ_R
1	T	/	0.15 mK	/	/	0.15 mK	/	/	0.15 mK	/
	ΔT	5.8	0.21 mK	3.6%	6.8	0.21 mK	3.1%	7.4	0.21 mK	2.8%
2	k	64	13.4	21%	64	13.4	21%	64	13.4	21%
1+2	ΔT_{EC}	0.35	0.074 K	**21%**	0.44	0.092 K	**21%**	0.48	0.10	**21%**

S5: Polarization vs. electric field loops at various frequencies

The unipolar polarization–electric field (*P*–*E*) hysteresis loops as-deposited and annealed PMN–35PT thick films were measured at room temperature using an aixACCT TF analyzer 2000 (aixACCT Systems GmbH, Germany). The single sinusoidal waveform with amplitude up to 500 kV·cm^{-1} and frequencies from 1 to 100 Hz was applied to top Au electrodes with the diameter of 1.5 mm (Figure S5). As the frequency decreases, the shape of the *P*–*E* hysteresis loops of the as-deposited thick films becomes round, indicating the influence of electrical conductivity. For thermally annealed films, the relaxor-ferroelectric shape of the *P*–*E* loops remains similar at all frequencies.

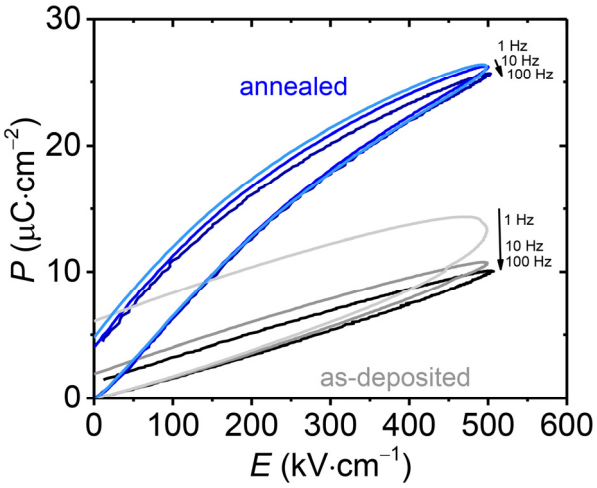

Figure S5: Unipolar *P*–*E* hysteresis loops of as-deposited (grey and black lines) and annealed (blue lines) PMN–35PT thick films. *P*–*E* loops were measured up to 500 kV·cm^{-1} and at frequencies from 1 to 100 Hz. Black arrows indicate increase in frequencies.

S6: Dielectric breakdown measurements – Weibull analysis

Dielectric breakdown measurements of as-deposited and annealed PMN–35PT thick films were performed using an aixACCT TF analyzer 2000 (aixACCT Systems GmbH, Germany) by applying a single sinusoidal unipolar waveform with a frequency of 100 Hz. To evaluate the dielectric breakdown fields (E_i), 17 Au top electrodes (1.5 mm diameter) of each sample were used. The evaluated E_i follow the two-parameter Weibull distribution described by [9], [10]:

$$X_i = \ln(E_i) \tag{S6.1}$$

$$Y_i = \ln(-\ln(1 - p_i)) \tag{S6.2}$$

$$p_i = \frac{i - 0.3}{N + 0.4} \tag{S6.3}$$

Here i, N and p_i represent the specimen sequential number, the sum of the tested specimens and the cumulative probability of dielectric breakdown, respectively. A high shape factor ($\beta > 1$), determined from the slope of the Weibull distribution (Figure S6), indicates low fluctuations of E_i in the as-deposited and annealed samples. The dielectric breakdown strength (DBS) is extracted from the intersection of the linear regression curve and the horizontal line $\ln(-\ln(1-p_i)) = 0$. It represents the electric field at which the breakdown probability is 63.2%.

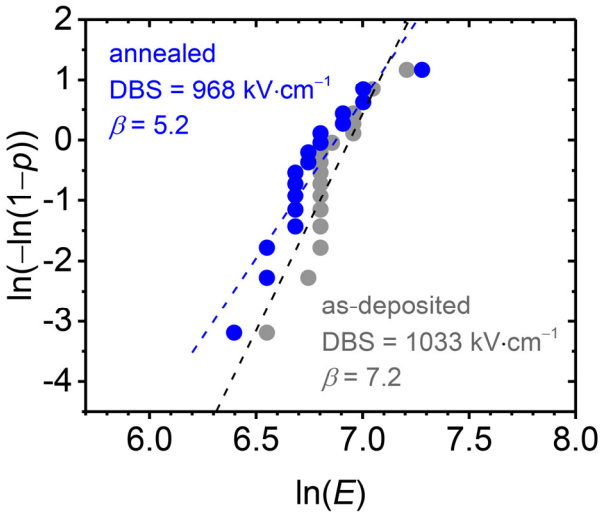

Figure S6: Weibull distribution of the dielectric breakdown field of as-deposited (marked grey) and annealed (blue) PMN–35PT thick films. The dashed lines represent linear regression.

S7: Dielectric properties as a function of temperature

The relative dielectric permittivity and dielectric losses (tan δ) were measured between 0 and 300 °C with a Precision LCR impedance meter (HP 4284A, Hewlett-Packard, CA, USA) in the frequency range 1–100 kHz. Figure S7 reveals a remarkable increase of dielectric permittivity after thermal annealing of PMN–35PT thick films at 400 °C. During heating, the dielectric permittivity of the as-deposited films increases, while the annealed films exhibit a broad frequency-dependent dielectric permittivity maximum at ~150 °C. The tan δ of thick films stays below 0.04, except for the as-deposited thick films at elevated temperatures (above ~200 °C). Note that the electrical response of as-deposited films is dominated by the defects, which are generated after AD. The reason for increase of tan δ with increasing temperature can be attributed to the relaxation of space charges, that become mobile at higher temperatures.

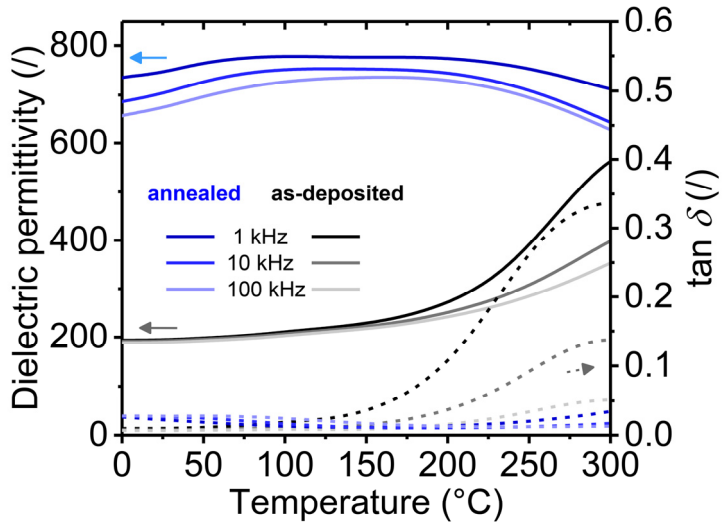

Figure S7: The relative dielectric permittivity (solid line) and tan δ (dashed line) vs. temperature of as-deposited (black-grey) and annealed (blue) PMN–35PT films.

Supporting video

The supporting video shows fatigue tensile bending tests of PMN–35PT thick films performed on a linear sliding moving stage and a custom made sample holder.

References

[1] L. Mao, Q. Meng, A. Ahmad, and Z. Wei, "Mechanical Analyses and Structural Design Requirements for Flexible Energy Storage Devices," *Adv. Energy Mater.*, vol. 7, no. 23, p. 1700535, 2017.

[2] S. Il Park, Y. Xiong, R. H. Kim, P. Elvikis, M. Meitl, D. H. Kim, J. Wu, J. Yoon, Y. Chang-Jae, Z. Liu, Y. Huang, K. C. Hwang, P. Ferreira, L. Xiuling, K. Choquette, J. A. Rogers, "Printed assemblies of inorganic light-emitting diodes for deformable and semitransparent displays," *Science*, vol. 325, no. 5943, pp. 977–981, 2009.

[3] F. Zhuo, U. Eckstein, N. H. Khansur, C. Dietz, D. Urushihara, T. Asaka, K. Kakimoto, K. G. Webber, X. Fang, and J. Rödel, "Temperature-induced changes of the electrical and mechanical properties of aerosol-deposited $BaTiO_3$ thick films for energy storage applications," *J. Am. Ceram. Soc.*, vol. 105, no. 6, pp. 4108–4121, 2022.

[4] H. Uršič, M. Hrovat, J. Holc, M. S. Zarnik, S. Drnovšek, S. Maček, and M. Kosec, "A large-displacement $65Pb(Mg_{1/3}Nb_{2/3})O_3$–$35PbTiO_3$/Pt bimorph actuator prepared by screen printing," *Sensors Actuators B Chem.*, vol. 133, no. 2, pp. 699–704, 2008.

[5] D. Faurie, P.-O. Renault, E. Le Bourhis, P. Villain, P. Goudeau, and F. Badawi, "Measurement of thin film elastic constants by X-ray diffraction," *Thin Solid Films*, vol. 469–470, pp. 201–205, 2004.

[6] DuPont, "DuPontTM Kapton® HN," electronics.dupont.com, 2021. https://www.dupont.com/content/dam/dupont/amer/us/en/products/ei-transformation/documents/DEC-Kapton-HN-datasheet.pdf.

[7] U. Prah, M. Sadl, A. Torello, P. Lheritier, V. Kovacova, H. Ursic, and E. Defay, "Direct electrocaloric characterization of ceramic films," under revision in *Small Methods*, 2023, available online: http://arxiv.org/abs/2302.06543.

[8] Z. Kutnjak, B. Rožič, and R. Pirc, "Electrocaloric Effect: Theory, Measurements, and Applications," in *Wiley Encyclopedia of Electrical and Electronics Engineering*, Hoboken: John Wiley & Sons, Inc., 2015.

[9] E. Tuncer, D. R. James, I. Sauers, A. R. Ellis, and M. O. Pace, "On dielectric breakdown statistics," *J. Phys. D. Appl. Phys.*, vol. 39, no. 19, pp. 4257–4268, 2006.

[10] J. Li, Z. Shen, X. Chen, S. Yang, W. Zhou, M. Wang, L. Wang, Q. Kou, Y. Liu, Q. Li, Z. Xu, Y. Chang, S. Zhang, and F. Li, "Grain-orientation-engineered multilayer ceramic capacitors for energy storage applications," *Nat. Mater.*, vol. 19, no. 9, pp. 999–1005, 2020.